




CSST forecast: impact from non-Gaussian covariances and requirements on systematics-control

Ji Yao¹, Huanyuan Shan^{1,2}, Ran Li³, Youhua Xu³, Dongwei Fan³, Dezi Liu⁴, Pengjie Zhang^{5,6,7}, Yu Yu^{5,6}, Bin Hu⁸, Nan Li³, Zuhui Fan⁹, Haojie Xu¹, Wuzheng Guo¹

¹Shanghai Astronomical Observatory (SHAO), Nandan Road 80, Shanghai, China

²University of Chinese Academy of Sciences, Beijing, China

³National Astronomical Observatory, Chinese Academy of Sciences, Beijing 100101, China

⁴South-Western Institute for Astronomy Research, Yunnan University, Kunming 650500, Yunnan, PR China

⁵Department of Astronomy, School of Physics and Astronomy, Shanghai Jiao Tong University, Shanghai, China

⁶Key Laboratory for Particle Astrophysics and Cosmology (MOE)/Shanghai Key Laboratory for Particle Physics and Cosmology, China

⁷Tsung-Dao Lee Institute, Shanghai Jiao Tong University, Shanghai, China

⁸Department of Astronomy, Beijing Normal University, Beijing 100875, China

⁹South-Western Institute for Astronomy Research, Yunnan University, Kunming 650500, China

Accepted XXX. Received YYY; in original form ZZZ

ABSTRACT

The precise estimation of the statistical errors and accurate removal of the systematical errors are the two major challenges for the stage IV cosmic shear surveys. We explore their impact for the China Space-Station Telescope (CSST) with survey area $\sim 17,500 \text{ deg}^2$ up to redshift ~ 4 . We consider statistical error contributed from Gaussian covariance, connected non-Gaussian covariance and super-sample covariance. We find the super-sample covariance can largely reduce the signal-to-noise of the two-point statistics for CSST, leading to a $\sim 1/3$ loss in the figure-of-merit for the matter clustering properties ($\sigma_8 - \Omega_m$ plane) and $1/6$ in the dark energy equation-of-state ($w_0 - w_a$ plane). We further put requirements of systematics-mitigation on: intrinsic alignment of galaxies, baryonic feedback, shear multiplicative bias, and bias in the redshift distribution, for an unbiased cosmology. The 10^{-2} to 10^{-3} level requirements emphasize strong needs in related studies, to support future model selections and the associated priors for the nuisance parameters.

Key words: weak lensing – cosmology – galaxy-galaxy lensing

1 INTRODUCTION

Weak gravitational lensing represents a fundamental tool for investigating cosmology, gravity, dark matter, and dark energy (Refregier 2003; Mandelbaum 2018). The synergy between weak gravitational lensing (WL) and cosmic microwave background (CMB) observations can yield even more robust results, as it possesses greater constraining power and effectively breaks parameter degeneracies (Planck Collaboration et al. 2020; DES Collaboration et al. 2021). Nonetheless, the tension observed between the cosmic microwave background (CMB) data at redshift $z \sim 1100$ and the results obtained from late-time galaxy surveys at $z < 1$, possibly caused by unexplained systematic errors or new physics beyond the Λ CDM cosmological model, poses a significant challenge when employing their combined analysis (Hildebrandt et al. 2017; Hamana et al. 2020; Hikage et al. 2019; Asgari et al. 2021; Heymans et al. 2021; DES Collaboration et al. 2021; Secco et al. 2022; Amon et al. 2021; Planck Collaboration et al. 2020). A broad range of investigations have been conducted to address the “ S_8 ” tension, encompassing diverse system-

atics (Yamamoto et al. 2022; Wright et al. 2020b; Yao et al. 2020, 2017; Kannawadi et al. 2019; Pujol et al. 2020; Mead et al. 2021; Secco et al. 2022; Amon et al. 2022; Fong et al. 2019), an array of statistical methods (Asgari et al. 2021; Joachimi et al. 2021; Lin & Ishak 2017; Harnois-Déraps et al. 2021; Shan et al. 2018; Sánchez et al. 2021; Leauthaud et al. 2022; Chang et al. 2019), and the possibility of new physics (Jedamzik et al. 2021). For further reading, we recommend consulting some recent review articles on this topic (Perivolaropoulos & Skara 2021; Mandelbaum 2018).

To comprehensively address the underlying causes of this tension, various cosmological probes are necessary owing to their distinct sensitivities to systematics and cosmology. Numerous recent observations are preparing to investigate an extended range of redshifts, sky patches, algorithms, and equipment properties. Prominent among these stage IV galaxy surveys are the Dark Energy Spectroscopic Instrument (DESI DESI Collaboration et al. 2016a,b), the Legacy Survey of Space and Time (LSST, LSST Science Collaboration et al. 2009) at the Vera C. Rubin Observatory, Euclid (Laureijs et al. 2011), Roman Space Telescope (also known as WFIRST, Spergel et al. 2015) and the China Space Station Telescope (CSST, Gong et al. 2019).

In this work, we investigate how accurately CSST can constrain cosmology using its cosmic shear two-point statistics. We test the

* E-mail: ji.yao@shao.ac.cn (JY)

† E-mail: hyshan@shao.ac.cn (HS)

impact from several important sources of statistical errors and systematic errors. More specifically, we investigate the loss of constraining power in terms of signal-to-noise ratio of the observables and figure-of-merit of the constrained parameters, due to the non-Gaussian covariances (Takada & Hu 2013; Joachimi et al. 2021). We investigate potential biases in cosmological parameters by analyzing different levels of residual bias in the mitigation of intrinsic alignment (Yao et al. 2020, 2017; Bridle & King 2007; Catelan et al. 2001; Hirata & Seljak 2004), baryonic feedback (Schneider & Teyssier 2015; Mead et al. 2015, 2021; Chen et al. 2023), shear multiplicative bias (Kannawadi et al. 2019; Mandelbaum et al. 2018; Giblin et al. 2021; Liu et al. 2021), and bias in the redshift distribution (Hildebrandt et al. 2021; Newman & Gruen 2022; van den Busch et al. 2020; Xu et al. 2022; Peng et al. 2022). We also provide calibration requirements to assist future studies in mitigating systematics.

This work is organized as follows. In Section 2 we briefly introduce the theoretical predictions to the observables, and the theories for different statistical errors and systematic errors. In Section 3 we describe the CSST data we expect. In Section 4 we forecast the cosmic shear measurements with tomography, and the impact of statistical errors and systematic errors on cosmological parameters. We summarize our findings in Section. 5.

2 THEORY

This section provides a brief review of the cosmic shear two-point statistics theory. We assume $\Omega_k = 0$ for spatial curvature, which renders the comoving radial distance and the comoving angular diameter distance identical.

2.2 Covariances

We consider three components of the covariance to account for the statistical error for cosmic shear:

$$\text{Cov}_{\text{tot}} = \text{Cov}_G + \text{Cov}_{\text{cNG}} + \text{Cov}_{\text{SSC}}, \quad (5)$$

namely, the Gaussian covariance, the connected non-Gaussian covariance, and the super-sample covariance.

The Gaussian covariance is based on a common assumption that the fluctuation of the underlying matter field is Gaussian. It is calculated by

$$\text{Cov}_G \left(C_{ij}^{\text{GG}}(\ell_1), C_{mn}^{\text{GG}}(\ell_2) \right) = \frac{\delta_{\ell_1, \ell_2}}{(2\ell + 1)\Delta\ell f_{\text{sky}}} \left[(C_{im}^{\text{GG}} + \delta_{i,m} N_{ii}^{\text{GG}})(C_{jn}^{\text{GG}} + \delta_{j,n} N_{jj}^{\text{GG}}) + (C_{in}^{\text{GG}} + \delta_{i,n} N_{ii}^{\text{GG}})(C_{jm}^{\text{GG}} + \delta_{j,m} N_{jj}^{\text{GG}}) \right], \quad (6)$$

where δ_{ℓ_1, ℓ_2} is the Kronecker delta function; C^{GG} is the shear-shear angular power spectrum; $N^{\text{GG}} = 4\pi f_{\text{sky}} \gamma_{\text{rms}}^2 / N_G$ is the shot noise for C^{GG} , where f_{sky} is the fraction of sky of the overlapped area, N_G is total number of the galaxies for the source.

The connected non-Gaussian covariance (Takada & Jain 2004) provides impact from non-Gaussian distribution of the density field due to late-time non-linear evolution, so that the higher order perturbation enters the covariance. It is calculated by

$$\text{Cov}_{\text{cNG}} \left(C_{ij}^{\text{GG}}(\ell_1), C_{mn}^{\text{GG}}(\ell_2) \right) = \int d\chi \frac{q_i(\chi) q_j(\chi) q_m(\chi) q_n(\chi)}{\chi^6} T_m \left(\frac{\ell_1 + 1/2}{\chi}, \frac{\ell_2 + 1/2}{\chi}, a(\chi) \right), \quad (7)$$

where T_m is the matter trispectrum, calculated using a halo model formalism (Joachimi et al. 2021). We adopt the NFW halo profile (Navarro et al. 1996) along with a concentration-mass relation (Duffy et al. 2008), a halo mass function (Tinker et al. 2008), and a halo bias (Tinker et al. 2010).

The super-sample covariance (Takada & Hu 2013; Takahashi et al. 2019) account for the selection effect of limited observational window, in which the background overdensity can deviate from the ensemble average of the Universe. It is calculated by

$$\text{Cov}_{\text{SSC}} \left(C_{ij}^{\text{GG}}(\ell_1), C_{mn}^{\text{GG}}(\ell_2) \right) = \int d\chi \frac{q_i(\chi) q_j(\chi) q_m(\chi) q_n(\chi)}{\chi^6} \frac{\partial P_\delta(\ell_1/\chi)}{\partial \delta_b} \frac{\partial P_\delta(\ell_2/\chi)}{\partial \delta_b} \sigma_b^2(\chi), \quad (8)$$

2.1 Cosmic shear

We employ the lensing convergence auto-correlation in Fourier space, i.e. the lensing angular power spectrum (Asgari et al. 2021),

$$C_{ij}^{\kappa\kappa}(\ell) = \int_0^{\chi_{\text{max}}} \frac{q_i(\chi) q_j(\chi)}{\chi^2} P_\delta \left(k = \frac{\ell + 1/2}{\chi}, z \right) d\chi, \quad (1)$$

which is a weighted projection from the 3D non-linear matter power spectrum $P_\delta(k, z)$ to the 2D galaxy-lensing convergence angular power spectrum $C^{\kappa\kappa}(\ell)$. It also depends on the comoving distance χ , and the lensing efficiency as a function of the lens position (given the distribution of the source galaxies) $q_s(\chi)$, which is written as

$$q_s(\chi_1) = \frac{3}{2} \Omega_m \frac{H_0^2}{c^2} (1 + z_1) \int_{\chi_1}^{\infty} n_s(\chi_s) \frac{(\chi_s - \chi_1) \chi_1}{\chi_s} d\chi_s, \quad (2)$$

where χ_s and χ_1 denote the comoving distance to the source and the lens, respectively, while $n_s(\chi_s) = n_s(z) dz/d\chi_s$ denotes the distribution of the source galaxies as a function of comoving distance. The “s” symbols for the source can be replaced by an index for different redshift bins, such as different tomographic bin index i or j .

The real-space shear-shear auto-correlation function can be obtained through the Hankel transformation

$$\xi_{+,ij}(\theta) = \frac{1}{2\pi} \int_0^\infty d\ell \ell C_{ij}^{\kappa\kappa}(\ell) J_0(\ell\theta), \quad (3)$$

$$\xi_{-,ij}(\theta) = \frac{1}{2\pi} \int_0^\infty d\ell \ell C_{ij}^{\kappa\kappa}(\ell) J_4(\ell\theta), \quad (4)$$

where $J_{0/4}(x)$ is the Bessel function of the first kind with order 0/4.

Therefore, by observing the correlation $\xi_{+/-,ij}$ or the shear-shear angular power spectrum $C_{ij}^{\text{GG}} = C_{ij}^{\kappa\kappa}$, we can derive the constraints on the cosmological parameters through Eq. (1), $P_\delta(k)$ and $\chi(z)$. To obtain a precise constraint on cosmology, many sources of statistical errors and systematic errors need to be considered.

where the derivative of $\partial P_\delta / \partial \delta_b$ gives the response of the matter power spectrum to a change of the background density contrast δ_b , while σ_b^2 denote the variance of the background matter fluctuations in the given footprint. Later we will show the footprint of the CSST cosmic shear observations, which is used to calculate σ_b^2 :

$$\sigma_b^2(\chi) = \frac{1}{A_{\text{eff},\mu} A_{\text{eff},\nu}} \sum_{\ell} P_{\delta}^{\text{lin}}\left(\frac{\ell}{\chi}\right) \sum_m a_{\ell m}^{\mu} a_{\ell m}^{\nu*}. \quad (9)$$

The A_{eff} is the effective area for the corresponding spherical harmonic coefficient $a_{\ell m}$ of a probe, with index μ or ν , and P_{δ}^{lin} is the linear matter power spectrum.

2.3 Systematics

In this work, we consider four major sources of systematics, which can potentially bias the observables at $\sim 10\%$ level if unaddressed, in the current Stage III surveys [Asgari et al. \(2021\)](#); [DES Collaboration et al. \(2021\)](#); [Hikage et al. \(2019\)](#). Other smaller systematics such as source clustering ([Yu et al. 2015](#)), beyond Born approximation ([Fabbian et al. 2018](#)), beyond Limber approximation ([Fang et al. 2020](#)), and potential CSST-based systematics (similar to [Euclid Collaboration et al. 2023b](#)) are left for future studies.

2.3.1 intrinsic alignment (IA)

Weak lensing uses the gravitationally lensed “optical” shape γ^G of the source galaxy to probe the matter and gravity of the lens. The “dynamical” shape of a galaxy before being lensed is affected by its local large-scale structures, causing the intrinsic alignment (IA) γ^I , which is therefore a source of systematics. Considering the shape noise γ^N , the overall observed shape reads

$$\gamma = \gamma^G + \gamma^I + \gamma^N. \quad (10)$$

Therefore, in two-point statistics, the target $\langle \gamma^G \gamma^G \rangle$ will be contaminated. In terms of the angular power spectrum,

$$C_{ij}^{\gamma\gamma} = C_{ij}^{\text{GG}} + C_{ij}^{\text{IG}} + C_{ij}^{\text{GI}} + C_{ij}^{\text{II}} + \delta_{i,j} C_{ii}^{\text{NN}}. \quad (11)$$

Here $C^{\gamma\gamma}$ is the observed angular power spectrum. C^{GG} is the target shear-shear power spectrum, which is identical to the convergence power spectrum as in Eq. (1). C^{IG} and C^{GI} are the shear-IA angular power spectra, which writes

$$C_{ij}^{\text{IG}}(\ell) = \int_0^{\chi_{\text{max}}} \frac{n_i(\chi) q_j(\chi)}{\chi^2} P_{\delta, \gamma^I} \left(k = \frac{\ell + 1/2}{\chi}, z \right) d\chi, \quad (12)$$

And C^{II} is the IA-IA angular power spectra, given by

$$C_{ij}^{\text{II}}(\ell) = \int_0^{\chi_{\text{max}}} \frac{n_i(\chi) n_j(\chi)}{\chi^2} P_{\gamma^I} \left(k = \frac{\ell + 1/2}{\chi}, z \right) d\chi, \quad (13)$$

The 3D matter-IA power spectrum P_{δ, γ^I} and the 3D IA power spectrum P_{γ^I} are based on IA physics. In this work, we use the most widely used NLA model ([Asgari et al. 2021](#); [DES Collaboration et al. 2021](#); [Hikage et al. 2019](#)):

$$P_{\delta, \gamma^I} = -A_{\text{IA}}(L, z) \frac{C_1 \rho_{\text{m},0}}{D(z)} P_{\delta}(k; \chi), \quad (14)$$

$$P_{\gamma^I} = \left(A_{\text{IA}}(L, z) \frac{C_1 \rho_{\text{m},0}}{D(z)} \right)^2 P_{\delta}(k; \chi), \quad (15)$$

which are both proportional to the non-linear matter power spectrum P_{δ} , suggesting that the IA is caused by the gravitational tidal field ([Catelan et al. 2001](#); [Hirata & Seljak 2004](#); [Bridle & King 2007](#)). It is also affected by $\rho_{\text{m},0} = \rho_{\text{crit}} \Omega_{\text{m},0}$ (the mean matter density of the universe at $z = 0$), the empirical amplitude

$C_1 = 5 \times 10^{-14} (h^2 M_{\text{sun}}/\text{Mpc}^{-3})$ taken from [Brown et al. \(2002\)](#), and $D(z)$, the linear growth factor normalized to $D(z = 0) = 1$. The IA amplitude A_{IA} can be luminosity-dependent ([Joachimi et al. 2011](#)) or redshift-dependent ([Chisari et al. 2016](#); [Samuroff et al. 2020](#); [Yao et al. 2020](#); [Tonegawa & Okumura 2021](#)).

The IA modeling in Eq. (14) and (15) can be replaced by more complicated models such as [Krause et al. \(2016\)](#); [Blazek et al. \(2017\)](#); [Fortuna et al. \(2020\)](#) for different galaxy samples ([Yao et al. 2020](#); [Samuroff et al. 2020](#); [Zjupa et al. 2020](#)). Its mitigation can alternatively be implemented with extra observables using self-calibration methods ([Zhang 2010b,a](#); [Yao et al. 2017, 2023b](#)).

2.3.2 baryonic feedback

The modeling of the matter power spectrum $P(k)$ normally uses N-body simulations ([Takahashi et al. 2012](#); [Euclid Collaboration et al. 2019](#)), so that the corresponding density profiles are the dark-matter-only case. The existence of baryonic matter and their associated non-gravitational and powerful process, so-called “baryonic feedback”, can further change the clustering features in $P(k)$, especially in the small-scales ([Jing et al. 2006](#); [Schneider & Teyssier 2015](#); [Mead et al. 2021](#)). The precise modeling of the baryonic feedback is essential for future cosmological observations ([Chen et al. 2023](#); [Aricò et al. 2020](#); [Martinelli et al. 2021](#)).

In this work, we examine the impact of residual baryonic feedback following the baryonic correction model (BCM, [Schneider & Teyssier 2015](#)):

$$P_{\text{BCM}}(k, z) = P_{\text{DM}}(k, z) F(k, z), \quad (16)$$

which alters the dark-matter-only power spectrum P_{DM} with a correction term F , written as

$$F(k, z) = G(k|M_c, \eta_b, z) S(k|k_s), \quad (17)$$

$$G(k|M_c, \eta_b, z) = \frac{B(z)}{1 + (k/k_g)^3} + [1 - B(z)], \quad (18)$$

$$S(k|k_s) = 1 + (k/k_s)^2. \quad (19)$$

Here $G(k|M_c, \eta_b, z)$ represents the suppression from gas dynamics, including AGN feedback, supernovae feedback, etc. $S(k|k_s)$ describes the increase of clustering at small-scale, due to central galaxy stars. Their further expansion for this fitting formula reads:

$$B(z) = B_0 \left[1 + \left(\frac{z}{z_c} \right)^{2.5} \right]^{-1}, \quad (20)$$

$$k_g(z) = \frac{0.7 [1 - B(z)]^4 \eta_b^{-1.6}}{h/\text{Mpc}}, \quad (21)$$

with the associated values $z_c = 2.3$, $B_0 = 0.105 \log_{10} \left[\frac{M_c}{\text{Mpc}/h} \right] - 1.27$, and model parameters $M_c = 10^{14.08} [\text{Mpc}/h]$ (mass scale), $\eta_b = 0.5$

(relation to the escape radius) and $k_s = 55$ [h/Mpc] (star component scale).

We consider the un-modeled residual bias in the matter power spectrum in the form of

$$\Delta P(k, z) = A_{\text{BCM}} [P_{\text{BCM}}(k, z) - P_{\text{DM}}(k, z)], \quad (22)$$

with an amplitude A_{BCM} to describe how precise we need to understand the true underlying baryonic physics.

2.3.3 shear multiplicative bias

The galaxy shear measurement can suffer from low signal-to-noise (S/N) of the dim galaxies and residuals from the point-spread-function (PSF) deconvolution (Zhang et al. 2023). In the first order, the measured/observed shear can be described as a linear distortion from the true shear:

$$\vec{\gamma}^{\text{obs}} = (1 + \mathbb{M}) \cdot \vec{\gamma}^{\text{true}} + \vec{c}, \quad (23)$$

where the 2-component column vector $\vec{\gamma}$ represents the combination of γ_i (with $i = 1, 2$), while \vec{c} represents the corresponding shear additive bias. The 2×2 matrix \mathbb{M} contains the shear multiplicative bias $m_{ij} = \partial\gamma_i^{\text{obs}}/\partial\gamma_j^{\text{true}}$. Generally, for the “gold” samples with good shear measurements, we have $|m| \ll 1$ and $|c| \ll |\gamma|$.

In this work, we consider the most common case of a homogeneous and isotropic multiplicative bias $m_{11} = m_{22} = m$, $m_{12} = m_{21} = 0$, and negligible additive bias $c_i = 0$, similar to the current Stage III observations can achieve (Asgari et al. 2021; Amon et al. 2021; Hikage et al. 2019). We note the non-vanishing additive bias can also be removed considering it mainly enters ξ_+ (Eq. 3) but not ξ_- (Eq. 4), or applying cross-correlations. Similarly, a z -dependent m can be further limited with cross-correlations (Liu et al. 2021; Yao et al. 2023a). In this case, the weak lensing power spectrum is changed by

$$\Delta C^{\text{GG}} = 2mC^{\text{GG}}. \quad (24)$$

2.3.4 bias in redshift distribution

As weak lensing requires a large amount of galaxies to suppress the intrinsic shape noise and subtract the cosmological lensing shear signals, photometric redshift (photo- z) is preferred over spectroscopic redshift (spec- z) for its low observational cost. However, the accuracy of photo- z does not satisfy the requirement for the current Stage III and future Stage IV weak lensing surveys, therefore careful calibration of the true redshift distribution is needed (Asgari et al. 2021; DES Collaboration et al. 2021; Wright et al. 2020a; Buchs et al. 2019; van den Busch et al. 2020; Xu et al. 2023; Alarcon et al. 2020).

The main impact of redshift accuracy on cosmology is the mean value of the source redshift distribution. Assume the mean value is biased by Δz , then the redshift distribution will change from $n(z)$ to $n(z - \Delta z)$, which changes the $n_s(\chi_s(z_s))$ and therefore the lensing efficiency q_s through Eq. (2) and the theoretical estimation of $C^{\kappa\kappa}$ through Eq. (1).

In this work, we consider a systematic shift in all redshift bins with the same amount Δz , which can lead to a systematic shift in all cosmological parameters. We note that the bias in redshift distribution is very sample-dependent, therefore the shift is in principle redshift-dependent. However, the z -dependent shift is highly based on the selection function of each specific survey, which is hard to put in the theoretical forecast. Also, the z -dependent bias can be easily identified with cross-correlations (van den Busch et al. 2020; Xu et al. 2023) or simply remove a certain z -bin (Asgari et al. 2021; Li et al.

2023). So for a concise demonstration, we use an identical z -bias in this work, which also strongly degenerates with the cosmology and is hard to detect.

2.4 Forecast

2.4.1 Fisher formalism

We use Fisher matrix (Yao et al. 2017; Clerkin et al. 2015; Kirk et al. 2012; Huterer et al. 2006; Coe 2009) to pass the statistical uncertainties of CSST observations to the cosmological parameters, to estimate the cosmological constraints and the potential bias from different residual systematics. The Fisher matrix is calculated as:

$$(F) = \left(\frac{\partial \vec{C}^{\kappa\kappa}}{\partial \vec{p}} \right)^T (\text{Cov}^{-1}) \left(\frac{\partial \vec{C}^{\kappa\kappa}}{\partial \vec{p}} \right), \quad (25)$$

where in between $()$ are all matrices. The vector $\vec{C}^{\kappa\kappa}$ is the column data-vector that contains all the i, j combinations and ℓ bins in Eq. (1), with total length of $N_{\text{data}} = [(N_{\text{tomo}} + 1)N_{\text{tomo}}]/2 \times N_{\ell}$, where N_{tomo} is the number of tomographic/redshift bins and N_{ℓ} is the number of angular bins. Its partial derivative with respect to the cosmological parameters \vec{p} , $\left(\frac{\partial \vec{C}^{\kappa\kappa}}{\partial \vec{p}} \right)$, is therefore a $N_{\text{data}} \times N_{\text{para}}$ matrix, with N_{para} correspond to the number of cosmological parameters. The inverse of the covariance (Cov^{-1}) uses to the covariance matrices introduced in Sec. 2.2, and is, therefore, a $N_{\text{data}} \times N_{\text{data}}$ matrix.

By using Eq. (25), we transform the covariance of the data vector to those of the cosmological parameters, with likelihood $-2\ln\mathcal{L} = \vec{p}^T (F) \vec{p}$. The $N_{\text{para}} \times N_{\text{para}}$ Fisher matrix F contains direct information of the variance on each parameter $\sigma_{\alpha}^2 = (F^{-1})_{\alpha\alpha}$ and the covariance between different parameters $\sigma_{\alpha\beta}^2 = (F^{-1})_{\alpha\beta}$. The constraining power in the two-parameter-space can also be evaluated with figure-of-merit (FoM), defined as $\text{FoM}_{\alpha\beta} = \left[\det(F^{-1})_{\alpha\beta} \right]^{-1/2}$

2.4.2 Biases due to residual systematics

To estimate how different residual biases can shift the best-fit cosmology, we first use the introduce systematics in Sec. 2.3 to estimate a residual bias $\Delta \vec{C}^{\kappa\kappa}$ in the data-vector. Then the corresponding shift in the cosmological parameters \vec{p} can be written as

$$\Delta \vec{p} = (F^{-1}) \left[\left(\frac{\partial \vec{C}^{\kappa\kappa}}{\partial \vec{p}} \right)^T (\text{Cov}^{-1}) (\Delta \vec{C}^{\kappa\kappa}) \right], \quad (26)$$

considering first order approximation to the likelihood (Yao et al. 2017; Huterer et al. 2006).

We note that in this work, we aim at getting a general requirement on the systematics, to guide future calibration works on different systematics. For some systematics such as IA and baryonic feedback, as the true model to describe the physics is still unknown, it is trivial to consider the marginalization over their nuisance parameters, due to different model’s parameters can have different degeneracies with the cosmological parameters. For any of the systematics mitigation methods, validation with simulation is also a crucial link, which can both estimate the potential residual bias and give priors to the nuisance parameters. Assuming the simulations can give strong enough priors, we no longer need to consider the constraining-power-loss due to marginalization.

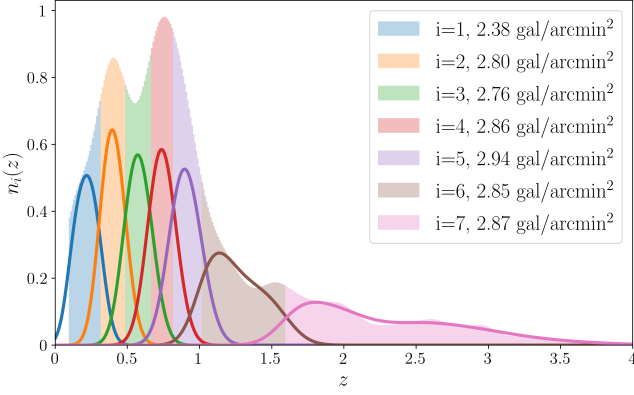


Figure 1. The tomographic redshift distribution for the forecast CSST gold lensing samples. The histogram is the photo- z distribution for different tomographic bins. The solid curves are the associated true- z distributions for each bin for the fiducial analysis, assuming no redshift bias. Galaxies with $z_p < 0.1$ are removed due to low lensing efficiency.

2.4.3 Signal-to-noise (S/N) definition

The conventional S/N definition uses amplitude fitting (Yao et al. 2023a). For a given measurement \vec{w}_{data} and an assumed theoretical model \vec{w}_{model} , we fit an amplitude A to the likelihood:

$$-2\ln\mathcal{L} = (\vec{w}_{\text{data}} - A\vec{w}_{\text{model}})^T (\text{Cov}^{-1}) (\vec{w}_{\text{data}} - A\vec{w}_{\text{model}}), \quad (27)$$

so that a posterior of $A_{-\sigma_A}^{+\sigma_A}$ can be obtained, where σ_A is the Gaussian standard deviation for the amplitude. Then the corresponding S/N is A/σ_A .

Under the frame of Fisher formalism, we have $\vec{w}_{\text{data}} = \vec{w}_{\text{model}}$ with a single free parameter A for the forecast. Similar to the procedures in Sec. 2.4.1, one can estimate the S/N is $A/\sigma_A =$

$$\sqrt{(\vec{w}_{\text{model}})^T (\text{Cov}^{-1}) (\vec{w}_{\text{model}})}.$$

3 SURVEY PROPERTIES

The China Space Station Telescope (CSST) is a space-based project aiming at mapping the Universe with both photometric and slitless spectroscopic observations, covering 17,500 deg² of the sky. Its imaging survey contains 7 photometric bands (NUV, u, g, r, i, z, y) with wavelength coverage from 255 nm to 1000 nm (Gong et al. 2019; Zhan 2021). The 5 σ point sources detection limit in nominal AB magnitude is $r \sim 26$ (Cao et al. 2018).

We present the CSST shear catalog properties for this forecast work. For reliable shear and photo- z measurements, we consider a reduction in the galaxy number density from 28 gal/arcmin² (Gong et al. 2019) to 20 gal/arcmin² (Liu et al. 2023) with appropriate S/N cuts. For more detailed studies considering blending and masking (Chang et al. 2013), it will require a PhoSim (Peterson et al. 2015)-like simulator that highly mimics the CSST galaxies, which is under development. However, the blending problem is less significant comparing with LSST (Liu et al. 2023).

In Fig. 1, we show the expected redshift distribution of the CSST source galaxies. The photo- z distribution is obtained by applying the CSST observational limits to the COSMOS photo- z galaxies (Cao et al. 2018; Ilbert et al. 2009). We divide the galaxies into 7 tomographic bins with (almost) equal numbers of galaxies, for higher

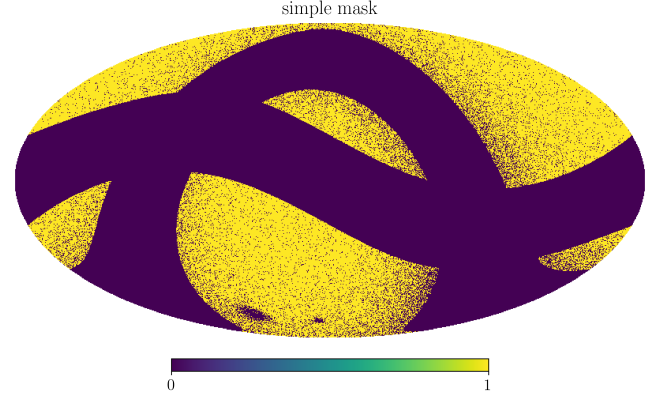


Figure 2. An illustration of the footprint for CSST cosmic shear forecast. After the masking of the galactic equator, the ecliptic equator, bright galaxies, and bright stars, the final footprint is reduced from ~ 17572 deg² to ~ 14877 deg². The area of this footprint will be used in the Gaussian covariance estimation (Eq. 6), and its geometry will be used in the super-sample covariance estimation (Eq. 8).

total S/N following Moskowitz et al. (2022). We remove galaxies with photo- z $z_p < 0.1$ as they contribute little to the total cosmological signals due to low lensing efficiency as in Eq. (2). We assume the true- z follows a Gaussian probability distribution function (PDF) around the photo- z , namely

$$p(z|z_p) = \frac{1}{\sqrt{2\pi}\sigma_z(1+z)} \exp \left\{ -\frac{(z - z_p - \Delta_z)^2}{2[\sigma_z(1+z)]^2} \right\}, \quad (28)$$

where we adapt the photo- z scatter $\sigma_z = 0.05$ and photo- z bias $\Delta_z = 0$ for the fiducial analysis (Cao et al. 2018). The resulting true- z distributions are also shown as the solid curves in Fig. 1. A non-vanishing photo- z bias Δ_z is equivalent to a systematic shift in the overall redshift distribution with Δ_z , introduced in Sec. 2.3.4.

We consider galaxy shape noise $\gamma_{\text{rms}} = 0.27$ that is close to the other stage IV surveys (Yao et al. 2017). It will enter the shot noise term N^{GG} as shown in Eq. (6). For a more detailed estimation of how much additional statistical error can be introduced from the shear measurement, a more realistic imaging simulation is needed to highly mimic the CSST galaxy properties.

We also estimate how the sky coverage will change considering simple masking of the bright galaxies and bright stars. We use a HEALPIX map (Górski et al. 2005; Zonca et al. 2019) with $N_{\text{side}} = 4096$ (~ 0.74 arcmin² per pixel) and remove the regions within $\pm 19.2^\circ$ of the galactic latitude and the ecliptic latitude. The remaining region is ~ 17572 deg², which approximates the CSST target sky. We further remove bright sources, which are likely to be low- z objects with low lensing efficiency and can contaminate their nearby galaxies. We remove pixels that contain any galaxy with a magnitude brighter than 18.5 (in B band from de Vaucouleurs et al. 1991), and any star with a magnitude brighter than 18 from GAIA DR3 (Gaia Collaboration et al. 2016, 2022). The resulting footprint is shown in Fig. 2, with the sky coverage reduced to ~ 14877 deg². The pixel size is significantly larger than the common size for bright object removal (Coupon et al. 2018), therefore the resulting footprint is a conservative estimation.

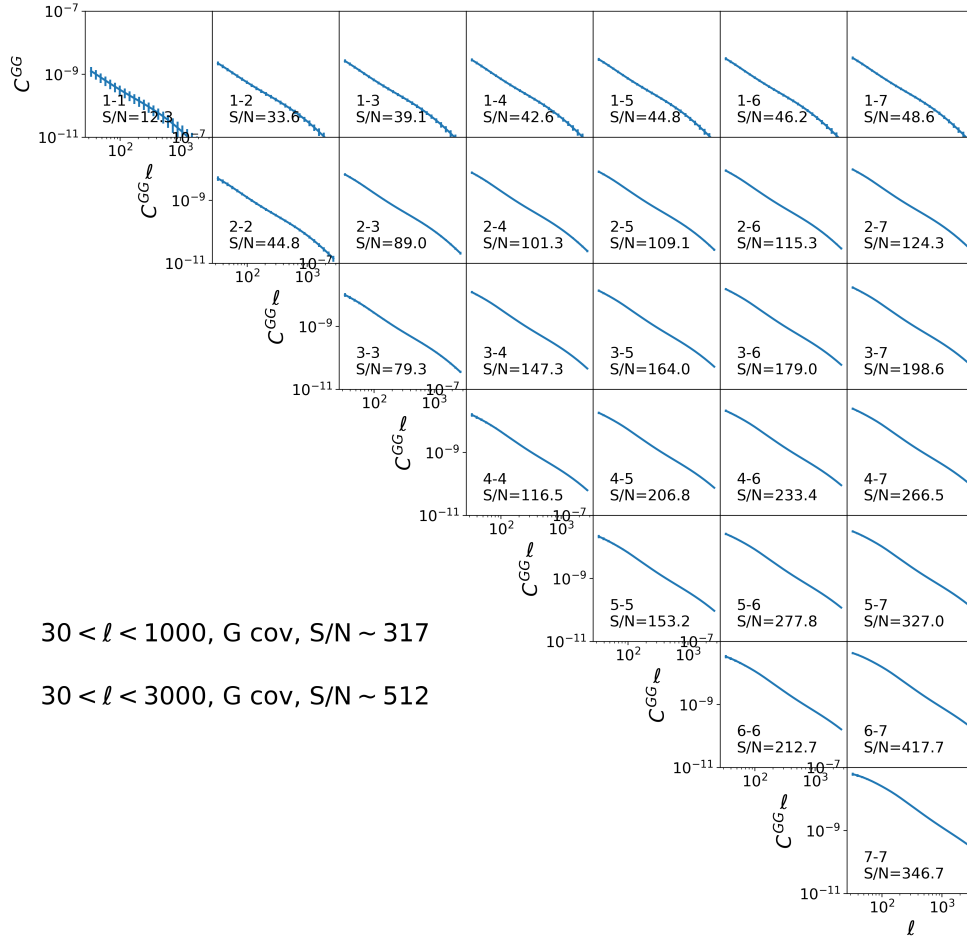


Figure 3. The tomographic shear-shear angular power spectra. In each subplot we present the $C_{ij}^{GG}(\ell)$ for the i -th and j -th bins. The Gaussian errorbars are presented following Eq. (6) and is very small for high- z high S/N bin pairs. The S/N is evaluated for each $i-j$ pair, while the total S/N is presented with Gaussian covariance. A comparison between Gaussian covariance and non-Gaussian covariance will be shown later in Fig. 4.

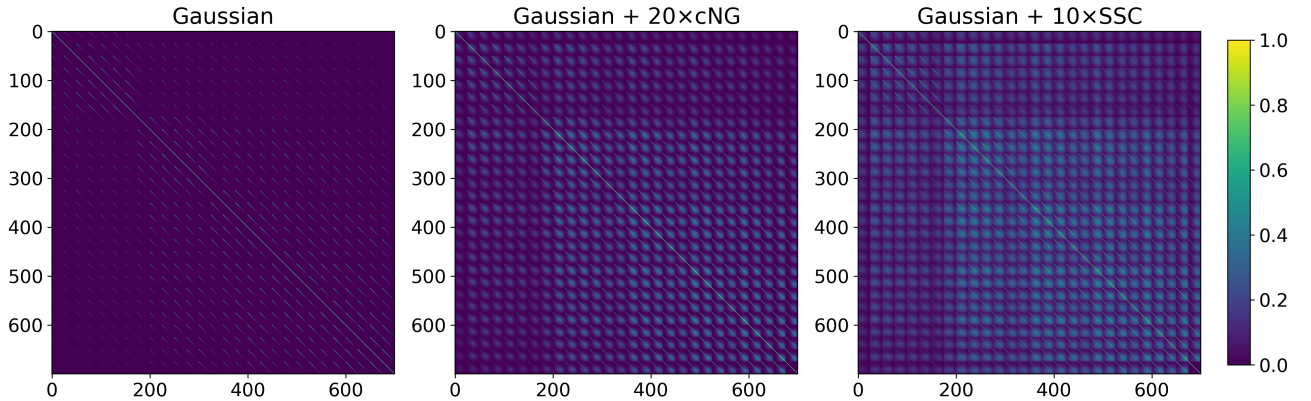


Figure 4. The impact from super-sample covariance (SSC). The left panel shows the normalized Gaussian covariance (or the correlation coefficient) for the data vector shown in Fig. 3, with a total length of ~ 700 for the fiducial cut. The right panel shows the comparison when adding the contribution from the SSC. It is clear the Gaussian+SSC case still has a major diagonal feature and many small off-diagonal features that are similar to the Gaussian covariance. However, the SSC additionally introduced strong off-diagonal features for $\ell_1 \neq \ell_2$ according to Eq. (8). This suggests the SSC does not significantly enlarge the errorbars in Fig. 3, but the introduced off-diagonal covariance can largely reduce the total S/N. We note the contribution from connected non-Gaussian (cNG) covariance is not observable if added to the above figures. For the fiducial cut $30 < \ell < 3000$, consider a total covariance of Gaussian+cNG+SSC, the total S/N will be reduced from ~ 512 to ~ 460 due to the strong off-diagonal covariance. For the conservative cut $30 < \ell < 1000$, the total S/N will reduce from ~ 317 to ~ 260 .

4 RESULTS

4.1 Statistics

We first study the statistical constraining power from cosmic shear. Two different scale cuts are applied: a fiducial scale cut with $30 < \ell < 3000$, and a conservative scale cut with $30 < \ell < 1000$ in case the small scale physics are not modeled correctly. We consider logarithmic angular binning with bin width $\Delta\ell = 0.2\ell$, following other stage IV surveys (Yao et al. 2017).

Based on the survey properties in Sec. 3, the tomographic cosmic shear angular power spectra can be calculated, shown in Fig. 3. Under the assumption of Gaussian covariance, we find a significantly high S/N of cosmic shear signal, with total S/N of ~ 512 and ~ 317 for the fiducial scale cut and the conservative scale cut, respectively.

We then compare the impact from the non-Gaussian covariances, as introduced in Eq. (7) and (8). We find that the connected non-Gaussian covariance has a much smaller contribution to the total covariance, compared with the Gaussian covariance and the super-sample covariance. The comparison is shown in Fig. 4. We find that the existence of SSC does not significantly increase the errorbars in Fig. 3. However, it introduces a significantly strong correlation between different data points, shown as the non-diagonal terms in the Gaussian+SSC case in Fig. 4.

The SSC is more dominant compared with the Gaussian covariance at small scales, shown in each small cube in the right panel of Fig. 4. Each cube corresponds to the covariance between a certain $C_{ij}^{GG}(\ell_1)$ v.s. $C_{mn}^{GG}(\ell_2)$ pair. The diagonal feature in each cube mainly comes from the Gaussian covariance ($\ell_1 = \ell_2$) and the off-diagonal features come from the SSC term. It can be seen that in many small cubes, the diagonal feature fade-away when it goes to a smaller scale (bottom-right corner). The finding of SSC being more dominant at small scales agrees with Takahashi et al. (2019).

When the total covariance including Gaussian+cNG+SSC is applied, S/N of the fiducial analysis will be reduced from ~ 512 to ~ 460 , mainly due to the contribution from SSC. This result also agrees with Takahashi et al. (2019) that SSC is a dominate statistical error in the next stage cosmic shear studies. Nonetheless, this reduced S/N is still much stronger than the current stage III observations can achieve (DES Collaboration et al. 2021).

We further show the cosmological constraints considering the Gaussian covariance only as well as the full covariance in Fig. 5. Similar to the S/N results, when considering the full covariance, the constraining power suffers from a significant loss compared with the case of using Gaussian covariance only. All the cosmological parameters, especially in the σ_8 v.s. Ω_m plane for the large-scale structure studies, and w_0 v.s. w_a plane for the dark energy equation of state, experience enlargement in the contour due to the SSC. Some FoM values are also calculated in Fig. 5. Overall, we conclude the impact of SSC is non-negligible for CSST cosmic shear studies.

4.2 Systematics

We study how different systematics can bias the cosmological results, considering four different systematics we are most interested in, see Sec. 2.3. For a certain type of residual systematics, its cosmological impact is quantified by Eq. (26). The statistical constraints are identical to Fig. 5, considering the full covariance with contribution from Gaussian, cNG, and SSC. We alter the residual amplitude for each systematics so that its maximum resulting shift in all parameter spaces is at a similar level as the 2σ contour, which is easier to see. The assumed residuals are $A_{IA} = 0.07$ for intrinsic alignment,

$m = 0.07$ for shear multiplicative bias, $A_{BCM} = 0.4$ for baryonic feedback, and $\Delta z = 0.012$ for mean redshift.

The residual systematical shift is shown in Fig. 6. It is clear that different residual $\Delta C(\ell)$ can bias the cosmology towards different directions with different amounts. We then raise requirements for the systematics-control based on those biases. We define two different tolerances: a visual tolerance and a probability tolerance.

(1) The visual tolerance, or the 68% contour tolerance, requires all the shifts to be within the boundary of the 1σ confidence contour for a certain type of systematics. This tolerance can be directly measured by changing the residual systematics in terms of $\{A_{IA}, m, A_{BCM}, \Delta z\}$, then observing its imprint in an updated bias shift figure, similar to Fig. 6. The actual measurements are shown in Fig. A1.

(2) The probability tolerance is 0.2 of the visual tolerance. This number comes from: the length of a $1\sigma_{2D}$ shift in the 2D contour correspond to ~ 1.52 times the $1\sigma_{1D}$ uncertainty in the 1D PDF (Coe 2009), while in 1D PDF, we require the bias to be $< 0.31\sigma_{1D}$ for a 95% overlap with the ideal 1D-PDF (Massey et al. 2013). Therefore the overall tolerance is $0.31\sigma_{1D} \frac{\sigma_{2D}}{1.52\sigma_{1D}} \sim 0.2\sigma_{2D}$, which we also refer to as the 95% probability tolerance.

We present the requirements for systematics-control for the CSST cosmic shear studies in Table 1. For different angular scale cuts, we show the requirements on the residual systematics in terms of the visual tolerance (68% contour) the probability tolerance (95% prob), and in which parameter space the tolerance is triggered (contaminated the most). The one with our fiducial cuts $30 < \ell < 3000$ requires a 95% probability tolerance presented at the bottom of the table. Generally, the allowed residual systematics are at 10^{-2} to 10^{-3} level of the full contamination, which is a very strong requirement for future systematics-mitigation works.

We notice the requirement on m changes very little for the two different scale cuts. This is because this limitation mainly comes from the $\Omega_m - \sigma_8$ plane, and when adding the information in $1000 < \ell < 3000$, the contour does not change much in the m -bias direction in Fig. 6. The main improvement comes from the direction that is perpendicular to the m -direction. Also, we note that our probability tolerance of $|m| < 0.0026$ is very close to the Euclid requirement of $|m| < 0.002$ (Laureijs et al. 2011), considering that we introduced the non-Gaussian covariances, which magnifies the $\Omega_m - \sigma_8$ plane contour size by a factor of ~ 1.5 .

We also notice that when adding the small-scale information, IA also starts to have more impact in the dark energy equation of state, becoming equivalent to the $\Omega_m - \sigma_8$ plane, see in Table 1. This also emphasizes the importance of considering IA at small-scales and its possible deviation from the assumed tidal alignment model (Blazek et al. 2015, 2017; Secco et al. 2022; Shi et al. 2021; Kurita et al. 2020; Fortuna et al. 2020; Zjupa et al. 2020).

5 CONCLUSIONS

In this work, we build a realistic set-up for the future CSST cosmic shear observation, and address the problem of how non-Gaussian covariances and residual systematics can change our cosmological analysis. We consider connected non-Gaussian covariance and super-sample covariance in terms of statistics, and residual systematics from intrinsic alignment, baryonic feedback, and measurements of shear multiplicative bias and mean redshift bias from $n(z)$ reconstruction. We obtained very strong requirements on the residuals, from 10^{-2} to 10^{-3} of the assumed contamination parameters, see in Table 1.

In terms of statistical errors, we demonstrated in Sec. 4.1 that

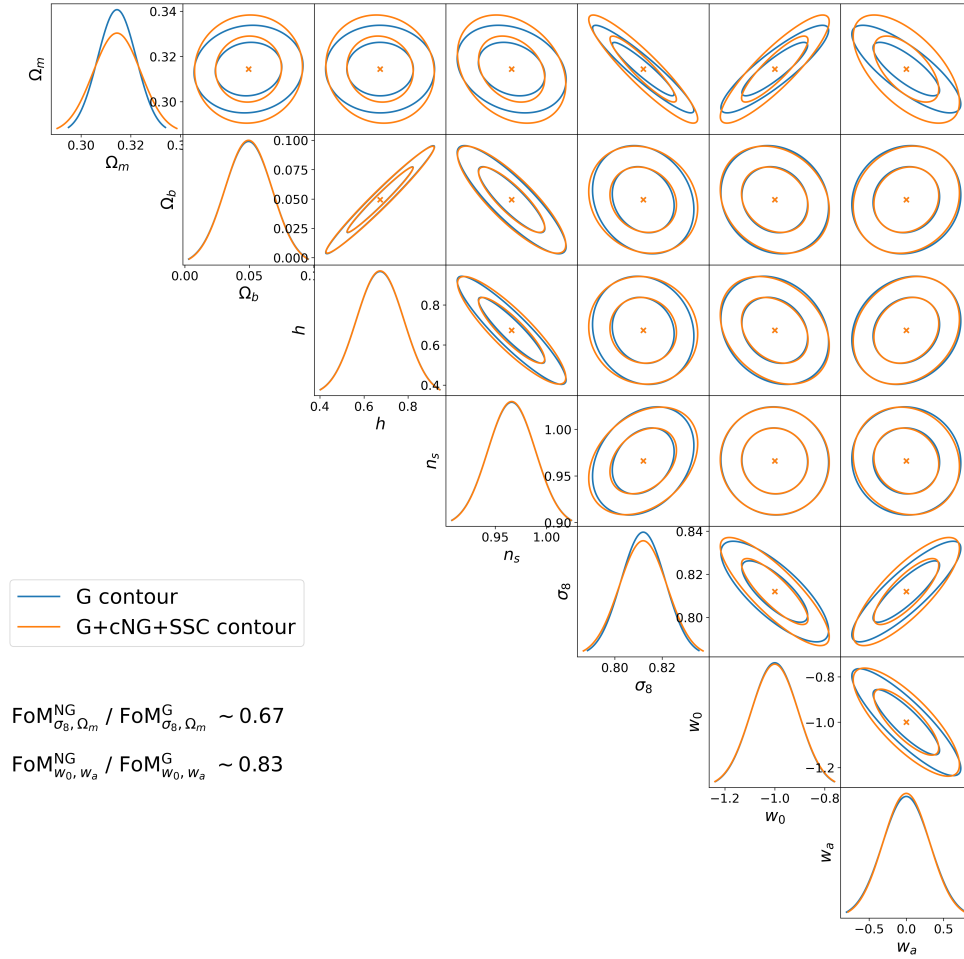


Figure 5. The forecasted cosmological constraints. The blue contours show the 1σ and 2σ confidence contours with Gaussian covariance only. When considering the full covariance, the strong off-diagonal terms in Fig. 4 will lead to a significant loss of constraining power, thus weaker constraints, shown in orange. The constraining power with the full covariance, estimated using figure-of-merit (FoM), is $\sim 2/3$ in the $\sigma_8 - \Omega_m$ plane and $\sim 1/6$ in the $w_0 - w_a$ plane comparing with the conventional Gaussian-covariance-only case. The numbers are ~ 0.70 and ~ 0.86 for $30 < \ell < 1000$.

Table 1. Requirements for systematics-control for CSST cosmic shear. We give an example of how to read this table. If we use $30 < \ell < 1000$ in the angular power spectra, when the residual bias of IA reaches $A_{\text{IA}} = 0.05$, in $\Omega_m - \sigma_8$ plane the shift will reach the 68% confidence contour. If we consider a bias towards this direction, it requires $A_{\text{IA}} < 0.01$ for the projected PDF in the bias direction to have a $> 95\%$ overlap with the ideal PDF. The last row gives our requirements that correspond to previous Euclid requirements (Massey et al. 2013; Laureijs et al. 2011) for the fiducial CSST analysis.

Case	A_{IA}	A_{BCM}	m	Δ_z
$\ell < 1000$, 68% contour	0.058	0.2	0.015	0.006
main constrain	$\Omega_m - \sigma_8$	$n_s - \Omega_b$	$\Omega_m - \sigma_8$	$\Omega_m - \sigma_8, \Omega_m - w_a$
$\ell < 1000$, 95% prob	0.012	0.04	0.003	0.0012
$\ell < 3000$, 68% contour	0.044	0.10	0.013	0.0042
main constrain	$\Omega_m - \sigma_8 - w_0 - w_a$	$n_s - \Omega_b$	$\Omega_m - \sigma_8$	$\Omega_m - w_0$
$\ell < 3000$, 95% prob	0.009	0.02	0.0026	0.0008

the impact from connected non-Gaussian (cNG) covariance is small, while super-sample covariance (SSC) has an important effect that can enlarge the 2D confidence contours of some key cosmological parameters, as seen in Fig. 5. We, therefore, emphasize the importance of taking it into consideration in future data analysis. We also suggest careful investigation of the SSC with real data considering $n(z)$ distribution and inhomogeneous galaxy distribution due to observational variation. The fact that SSC depends on the survey footprint

also suggests that in order to maximize the scientific outcome for early-stage CSST data, the design of the survey strategy to minimize SSC is important.

In terms of systematical errors, we considered how different systematics can bias the cosmological results in different ways, shown in Fig. 6. We use the 2D parameter space which is mostly affected by a certain type of systematics to describe the tolerance level of the residual bias. This approach is different from the conventional anal-

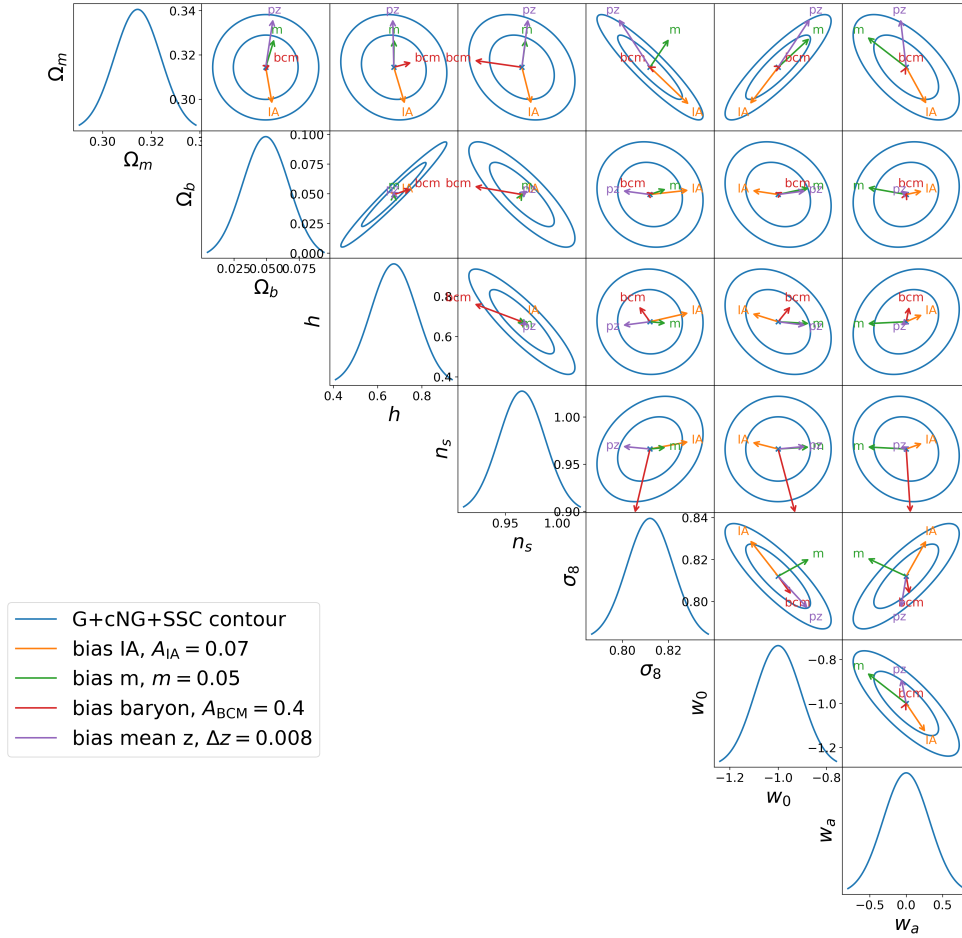


Figure 6. Systematical shifts due to different sources of residual systematics introduced in Sec. 2.3. The types and amplitudes of the residual systematics are shown in the labels, and how they can bias the cosmology, in terms of direction and amount, are shown as the arrows. The contours are the 1σ and 2σ uncertainties with the full covariance. We note this figure works as a demonstration of the systematics, and a tool to raise requirements on the systematics-control, presented in Table 1.

yses which normally focus on the bias in the dark energy equation of state (Massey et al. 2013). However, we still have comparable requirements in terms of shear multiplicative bias. The strong requirements for future CSST systematics-control are beyond the current constraints on those effects (Yao et al. 2017, 2023b; Schneider & Teyssier 2015; Chen et al. 2023; Asgari et al. 2021; DES Collaboration et al. 2021; Peng et al. 2022; Xu et al. 2023). Therefore, we emphasize the importance of pushing new techniques, developing realistic simulations, and combining different approaches (Alarcon et al. 2020) to further constrain those systematics.

We also notice in this analysis, we do not consider the marginalization of the nuisance parameters, which can potentially lead to a loss of constraining power. This is because, for different systematics models, the nuisance parameters could degenerate in different ways with the cosmological model, leading to different constraining power (DES Collaboration et al. 2021). Also, what kind of models are sufficient will base on future studies with high-fidelity simulations and high S/N measurements from the data. If the future investigation can put strong enough constraints on the nuisance parameters, there will not be any significant constraining power loss. Finally, the enlargement due to marginalization will only lose the requirements, so ignoring it will not sabotage the above calibration targets.

The studies here primarily concern the cosmic-shear two-point

correlation analyses. To fully utilise the CSST weak lensing data for cosmological constraints, other statistical tools beyond the two-point correlations are necessary (Euclid Collaboration et al. 2023a; Shan et al. 2018; Martinet et al. 2021). The impact of the systematics on these alternative statistics deserve further careful investigations (Yuan et al. 2019; Zhang et al. 2022; Harnois-Déraps et al. 2021).

ACKNOWLEDGEMENTS

This work is supported by National Key R&D Program of China No. 2022YFF0503403. JY acknowledges the support from NSFC Grant No.12203084, the China Postdoctoral Science Foundation Grant No. 2021T140451, and the Shanghai Post-doctoral Excellence Program Grant No. 2021419. HYS acknowledges the support from NSFC of China under grant 11973070, the Shanghai Committee of Science and Technology grant No.19ZR1466600 and Key Research Program of Frontier Sciences, CAS, Grant No. ZDBS-LY-7013. PZ acknowledges the support of NSFC No. 11621303, the National Key R&D Program of China 2020YFC22016. ZF acknowledges the support from NSFC No. 11933002 and U1931210. We acknowledge the support from the science research grants from the China Manned Space Project with NO. CMS-CSST-2021-A01, CMS-CSST-2021-A02, NO. CMS-CSST-2021-B01 and NO. CMS-CSST-2021-B04.

We acknowledge the usage of the following packages `pycel`¹, `healpy`², `matplotlib`³, `astropy`⁴, `scipy`⁵ for their accurate and fast performance and all their contributed authors.

This work has made use of data from the European Space Agency (ESA) mission *Gaia* (<https://www.cosmos.esa.int/gaia>), processed by the *Gaia* Data Processing and Analysis Consortium (DPAC, <https://www.cosmos.esa.int/web/gaia/dpac/consortium>). Funding for the DPAC has been provided by national institutions, in particular the institutions participating in the *Gaia* Multilateral Agreement.

DATA AVAILABILITY

REFERENCES

- Alarcon A., Sánchez C., Bernstein G. M., Gaztañaga E., 2020, *MNRAS*, **498**, 2614
- Amon A., et al., 2021, arXiv e-prints, p. [arXiv:2105.13543](https://arxiv.org/abs/2105.13543)
- Amon A., et al., 2022, *Phys. Rev. D*, **105**, 023514
- Aricò G., Angulo R. E., Hernández-Montegudo C., Contreras S., Zennaro M., Pellejero-Ibañez M., Rosas-Guevara Y., 2020, *MNRAS*, **495**, 4800
- Asgari M., et al., 2021, *A&A*, **645**, A104
- Astropy Collaboration et al., 2013, *A&A*, **558**, A33
- Blazek J., Vlah Z., Seljak U., 2015, *J. Cosmology Astropart. Phys.*, **8**, 015
- Blazek J., MacCrann N., Troxel M. A., Fang X., 2017, preprint, ([arXiv:1708.09247](https://arxiv.org/abs/1708.09247))
- Bridle S., King L., 2007, *New Journal of Physics*, **9**, 444
- Brown M. L., Taylor A. N., Hambly N. C., Dye S., 2002, *MNRAS*, **333**, 501
- Buchs R., et al., 2019, *MNRAS*, **489**, 820
- Cao Y., et al., 2018, *MNRAS*, **480**, 2178
- Catelan P., Kamionkowski M., Blandford R. D., 2001, *MNRAS*, **320**, L7
- Chang C., et al., 2013, *MNRAS*, **434**, 2121
- Chang C., et al., 2019, *MNRAS*, **482**, 3696
- Chen A., et al., 2023, *MNRAS*, **518**, 5340
- Chisari N., et al., 2016, *MNRAS*, **461**, 2702
- Chisari N. E., et al., 2019, *ApJS*, **242**, 2
- Clerkin L., Kirk D., Lahav O., Abdalla F. B., Gaztañaga E., 2015, *MNRAS*, **448**, 1389
- Coe D., 2009, arXiv e-prints, p. [arXiv:0906.4123](https://arxiv.org/abs/0906.4123)
- Coupon J., Czakon N., Bosch J., Komiyama Y., Medezinski E., Miyazaki S., Oguri M., 2018, *PASJ*, **70**, S7
- DES Collaboration et al., 2021, arXiv e-prints, p. [arXiv:2105.13549](https://arxiv.org/abs/2105.13549)
- DESI Collaboration et al., 2016a, arXiv e-prints, p. [arXiv:1611.00036](https://arxiv.org/abs/1611.00036)
- DESI Collaboration et al., 2016b, arXiv e-prints, p. [arXiv:1611.00037](https://arxiv.org/abs/1611.00037)
- Duffy A. R., Schaye J., Kay S. T., Dalla Vecchia C., 2008, *MNRAS*, **390**, L64
- Euclid Collaboration et al., 2019, *MNRAS*, **484**, 5509
- Euclid Collaboration et al., 2023a, arXiv e-prints, p. [arXiv:2301.12890](https://arxiv.org/abs/2301.12890)
- Euclid Collaboration et al., 2023b, arXiv e-prints, p. [arXiv:2302.04507](https://arxiv.org/abs/2302.04507)
- Fabbian G., Calabrese M., Carbone C., 2018, *J. Cosmology Astropart. Phys.*, **2018**, 050
- Fang X., Krause E., Eifler T., MacCrann N., 2020, *J. Cosmology Astropart. Phys.*, **2020**, 010
- Fong M., Choi M., Catlett V., Lee B., Peel A., Bowyer R., King L. J., McCarthy I. G., 2019, *MNRAS*, **488**, 3340
- Fortuna M. C., Hoekstra H., Joachimi B., Johnston H., Chisari N. E., Georgiou C., Mahony C., 2020, arXiv e-prints, p. [arXiv:2003.02700](https://arxiv.org/abs/2003.02700)
- Gaia Collaboration et al., 2016, *A&A*, **595**, A1
- Gaia Collaboration et al., 2022, arXiv e-prints, p. [arXiv:2208.00211](https://arxiv.org/abs/2208.00211)
- Giblin B., et al., 2021, *A&A*, **645**, A105
- Gong Y., et al., 2019, *ApJ*, **883**, 203
- Górski K. M., Hivon E., Banday A. J., Wandelt B. D., Hansen F. K., Reinecke M., Bartelmann M., 2005, *ApJ*, **622**, 759
- Hamana T., et al., 2020, *PASJ*, **72**, 16
- Harnois-Déraps J., Martinet N., Castro T., Dolag K., Giblin B., Heymans C., Hildebrandt H., Xia Q., 2021, *MNRAS*, **506**, 1623
- Heymans C., et al., 2021, *A&A*, **646**, A140
- Hikage C., et al., 2019, *PASJ*, **71**, 43
- Hildebrandt H., et al., 2017, *MNRAS*, **465**, 1454
- Hildebrandt H., et al., 2021, *A&A*, **647**, A124
- Hirata C. M., Seljak U., 2004, *Phys. Rev. D*, **70**, 063526
- Hunter J. D., 2007, *Computing in Science & Engineering*, **9**, 90
- Huterer D., Takada M., Bernstein G., Jain B., 2006, *MNRAS*, **366**, 101
- Ilbert O., et al., 2009, *ApJ*, **690**, 1236
- Jedamzik K., Pogosian L., Zhao G.-B., 2021, *Communications Physics*, **4**, 123
- Jing Y. P., Zhang P., Lin W. P., Gao L., Springel V., 2006, *ApJ*, **640**, L119
- Joachimi B., Mandelbaum R., Abdalla F. B., Bridle S. L., 2011, *A&A*, **527**, A26
- Joachimi B., et al., 2021, *A&A*, **646**, A129
- Jones E., Oliphant T., Peterson P., et al., 2001–, SciPy: Open source scientific tools for Python, <http://www.scipy.org/>
- Kannawadi A., et al., 2019, *A&A*, **624**, A92
- Kirk D., Rassat A., Host O., Bridle S., 2012, *MNRAS*, **424**, 1647
- Krause E., Eifler T., Blazek J., 2016, *MNRAS*, **456**, 207
- Kurita T., Takada M., Nishimichi T., Takahashi R., Osato K., Kobayashi Y., 2020, arXiv e-prints, p. [arXiv:2004.12579](https://arxiv.org/abs/2004.12579)
- LSST Science Collaboration et al., 2009, arXiv e-prints, p. [arXiv:0912.0201](https://arxiv.org/abs/0912.0201)
- Laureijs R., et al., 2011, arXiv e-prints, p. [arXiv:1110.3193](https://arxiv.org/abs/1110.3193)
- Leauthaud A., et al., 2022, *MNRAS*, **510**, 6150
- Li X., et al., 2023, arXiv e-prints, p. [arXiv:2304.00702](https://arxiv.org/abs/2304.00702)
- Lin W., Ishak M., 2017, *Phys. Rev. D*, **96**, 083532
- Liu X., Liu D., Gao Z., Wei C., Li G., Fu L., Futamase T., Fan Z., 2021, *Phys. Rev. D*, **103**, 123504
- Liu D. Z., et al., 2023, *A&A*, **669**, A128
- Mandelbaum R., 2018, *ARA&A*, **56**, 393
- Mandelbaum R., et al., 2018, *PASJ*, **70**, S25
- Martinelli M., et al., 2021, *A&A*, **649**, A100
- Martinet N., Harnois-Déraps J., Jullo E., Schneider P., 2021, *A&A*, **646**, A62
- Massey R., et al., 2013, *MNRAS*, **429**, 661
- Mead A. J., Peacock J. A., Heymans C., Joudaki S., Heavens A. F., 2015, *MNRAS*, **454**, 1958
- Mead A. J., Brieden S., Tröster T., Heymans C., 2021, *MNRAS*, **502**, 1401
- Moskowitz I., Gawiser E., Bault A., Broussard A., Newman J. A., Zuntz J., The LSST Dark Energy Science Collaboration 2022, arXiv e-prints, p. [arXiv:2212.06754](https://arxiv.org/abs/2212.06754)
- Navarro J. F., Frenk C. S., White S. D. M., 1996, *ApJ*, **462**, 563
- Newman J. A., Gruen D., 2022, *ARA&A*, **60**, 363
- Peng H., Xu H., Zhang L., Chen Z., Yu Y., 2022, *MNRAS*, **516**, 6210
- Perivolaropoulos L., Skara F., 2021, arXiv e-prints, p. [arXiv:2105.05208](https://arxiv.org/abs/2105.05208)
- Peterson J. R., et al., 2015, *ApJS*, **218**, 14
- Planck Collaboration et al., 2020, *A&A*, **641**, A1
- Pujol A., Bobin J., Sureau F., Guinot A., Kilbinger M., 2020, arXiv e-prints, p. [arXiv:2006.07011](https://arxiv.org/abs/2006.07011)
- Refregier A., 2003, *ARA&A*, **41**, 645
- Samuroff S., Mandelbaum R., Blazek J., 2020, arXiv e-prints, p. [arXiv:2009.10735](https://arxiv.org/abs/2009.10735)
- Sánchez C., et al., 2021, arXiv e-prints, p. [arXiv:2105.13542](https://arxiv.org/abs/2105.13542)
- Schneider A., Teyssier R., 2015, *J. Cosmology Astropart. Phys.*, **2015**, 049
- Secco L. F., et al., 2022, *Phys. Rev. D*, **105**, 023515
- Shan H., et al., 2018, *MNRAS*, **474**, 1116
- Shi J., Kurita T., Takada M., Osato K., Kobayashi Y., Nishimichi T., 2021, *J. Cosmology Astropart. Phys.*, **2021**, 030
- Spergel D., et al., 2015, arXiv e-prints, p. [arXiv:1503.03757](https://arxiv.org/abs/1503.03757)
- Takada M., Hu W., 2013, *Phys. Rev. D*, **87**, 123504
- Takada M., Jain B., 2004, *MNRAS*, **348**, 897

- Takahashi R., Sato M., Nishimichi T., Taruya A., Oguri M., 2012, *ApJ*, **761**, 152
- Takahashi R., Nishimichi T., Takada M., Shirasaki M., Shiroshima K., 2019, *MNRAS*, **482**, 4253
- Tinker J., Kravtsov A. V., Klypin A., Abazajian K., Warren M., Yepes G., Gottlöber S., Holz D. E., 2008, *ApJ*, **688**, 709
- Tinker J. L., Robertson B. E., Kravtsov A. V., Klypin A., Warren M. S., Yepes G., Gottlöber S., 2010, *ApJ*, **724**, 878
- Tonegawa M., Okumura T., 2021, arXiv e-prints, p. [arXiv:2109.14297](#)
- Wright A. H., Hildebrandt H., van den Busch J. L., Heymans C., 2020a, *A&A*, **637**, A100
- Wright A. H., Hildebrandt H., van den Busch J. L., Heymans C., Joachimi B., Kannawadi A., Kuijken K., 2020b, *A&A*, **640**, L14
- Xu H., et al., 2022, arXiv e-prints, p. [arXiv:2209.03967](#)
- Xu H., et al., 2023, *MNRAS*,
- Yamamoto M., Troxel M. A., Jarvis M., Mandelbaum R., Hirata C., Long H., Choi A., Zhang T., 2022, arXiv e-prints, p. [arXiv:2203.08845](#)
- Yao J., Ishak M., Lin W., Troxel M. A., 2017, preprint, ([arXiv:1707.01072](#))
- Yao J., Shan H., Zhang P., Kneib J.-P., Jullo E., 2020, *ApJ*, **904**, 135
- Yao J., et al., 2023a, *arXiv e-prints*, p. [arXiv:2301.13434](#)
- Yao J., et al., 2023b, *arXiv e-prints*, p. [arXiv:2301.13437](#)
- Yu Y., Zhang P., Lin W., Cui W., 2015, *ApJ*, **803**, 46
- Yuan S., Pan C., Liu X., Wang Q., Fan Z., 2019, *ApJ*, **884**, 164
- Zhan H., 2021, *Chinese Science Bulletin*, **66**, 1290
- Zhang P., 2010a, *MNRAS*, **406**, L95
- Zhang P., 2010b, *ApJ*, **720**, 1090
- Zhang T., Liu X., Wei C., Li G., Luo Y., Kang X., Fan Z., 2022, *ApJ*, **940**, 96
- Zhang Z., Shan H., Li N., Wei C., Yao J., Li R., 2023, *arXiv e-prints*, p. [arXiv:2301.02986](#)
- Zjupa J., Schäfer B. M., Hahn O., 2020, arXiv e-prints, p. [arXiv:2010.07951](#)
- Zonca A., Singer L., Lenz D., Reinecke M., Rosset C., Hivon E., Gorski K., 2019, *Journal of Open Source Software*, **4**, 1298
- de Vaucouleurs G., de Vaucouleurs A., Corwin Herold G. J., Buta R. J., Paturel G., Fouque P., 1991, Third Reference Catalogue of Bright Galaxies
- van den Busch J. L., et al., 2020, *A&A*, **642**, A200

APPENDIX A: THE 68% CONTOUR TOLERANCES

We show the 68% contour tolerances for the systematics in Fig. A1. The maximum shifts are right on the edge of the contours, while the values of the parameters correspond to the 68% contour tolerances with $30 < \ell < 3000$ in Table 1. We note the tips of the arrows in Fig. 6 are not very accurate, and are only for exhibition. Here we use Fig. A1 to show the actual values.

This paper has been typeset from a \LaTeX file prepared by the author.

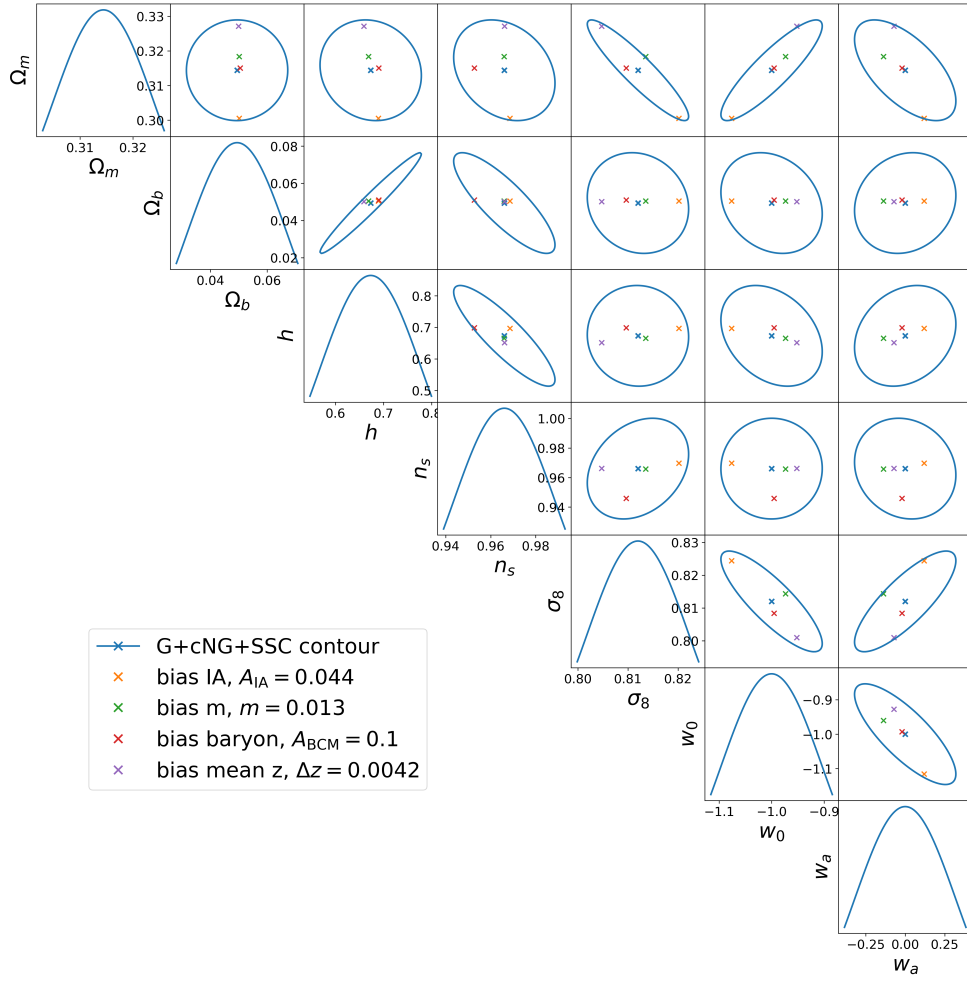


Figure A1. The 68% contour tolerances are measured when all the shifts are within the 1σ contour, with the maximum shift right on the edge. In this figure, we use “x” to measure the shift, while the arrows in Fig. 6 are for presentational purposes.